Secondary phases characterization by SANS and XAS of an ODS ferritic steel after thermal aging at 873 K

Oñoro, M.; Parnell, S.R.; Salas-Colera, E.; Alba Venero, D.; Martin-Diaconesu, V.; Leguey, T.; de Castro, V.; Auger, M.A.

DOI
10.1016/j.nme.2024.101671

Publication date
2024

Document Version
Final published version

Published in
Nuclear Materials and Energy

Citation (APA)
Oñoro, M., Parnell, S. R., Salas-Colera, E., Alba Venero, D., Martin-Diaconesu, V., Leguey, T., de Castro, V., & Auger, M. A. (2024). Secondary phases characterization by SANS and XAS of an ODS ferritic steel after thermal aging at 873 K. *Nuclear Materials and Energy*, *39*, Article 101671. https://doi.org/10.1016/j.nme.2024.101671

Nuclear Materials and Energy 39 (2024) 101671

Contents lists available at ScienceDirect

Nuclear Materials and Energy

journal homepage: www.elsevier.com/locate/nme

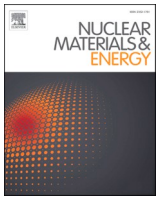

Secondary phases characterization by SANS and XAS of an ODS ferritic steel after thermal aging at 873 K

M. Oñoro [a,*], S.R. Parnell [b], E. Salas-Colera [a], D. Alba Venero [c], V. Martin-Diaconesu [d], T. Leguey [a], V. de Castro [a], M.A. Auger [a]

[a] Department of Physics, Universidad Carlos III de Madrid, Av. de la Universidad 30, 28911 Leganés, Madrid, Spain
[b] Faculty of Applied Sciences, Delft University of Technology, Mekelweg 15, 2629 JB Delft, the Netherlands
[c] ISIS Neutron and Muon Facility, Rutherford Appleton Laboratory, Didcot OX11 0QX, United Kingdom
[d] ALBA Synchrotron – CELLS, Carrer de la Llum 2-26, 08290 Cerdanyola del Vallès, Barcelona, Spain

ARTICLE INFO

Keywords:
ODS steel
Structural material
Aging
Laves phase
Nanoparticles
SANS
XAS

ABSTRACT

An ODS steel with nominal composition Fe–14Cr–2W–0.4Ti-0.3Y_2O_3 (wt.%) was produced by mechanical alloying and compacted by hot isostatic pressing (HIP) followed by hot cross rolling (HCR). To check the effects of thermal aging at relevant temperatures of operation in fusion power plants, the alloy was thermally aged at 873 K for 2000 h. In this work, small-angle neutron scattering (SANS) and X-ray absorption spectroscopy (XAS) techniques are used for the advanced characterization of secondary phases and the oxide nanoparticle dispersion. SANS results show that the oxide nanoparticles remain stable after the thermal aging treatment. Composition of the oxide nanoparticles was identified as Y_2TiO_5 or $Y_2Ti_2O_7$ by SANS, while non-stoichiometry was found by XAS analysis. Laves phase precipitation after the thermal aging treatment is further confirmed by SANS, from the magnetic anisotropic contribution to the scattering intensity associated to this metallic phase, and by XANES.

1. Introduction

Structural materials research is a major topic for the development of the nuclear energy sector. Oxide dispersion strengthened (ODS) reduced activated ferritic (RAF) steels (12–16 Cr wt.%) are leading structural material candidates for nuclear fusion applications. They are characterized by their enhanced performance at elevated operating temperatures, up to 1073 K, and high resistance to high neutron doses, swelling or He embrittlement [1,2]. A core strengthening mechanism in ODS steels relies on the homogeneous dispersion of oxide nanoparticles in the steel matrix [3]. The top performance of ODS steels is based on achieving the best homogeneous dispersion of nano-oxides, resulting in high tensile strength and good ductility at the expected reactor operational temperatures [4].

The homogeneous nanosized dispersion of Y-rich nanoprecipitates in the material under study has been previously characterized by advanced high-resolution techniques: transmission electron microscopy (TEM) and atom probe tomography (APT) [5]. $M_{23}C_6$ precipitates and titanium oxides were observed before and after thermal aging, while Laves phase precipitated at grain boundaries during the aging treatment. A homogeneous and stable distribution of Y-Ti-rich nanoprecipitates was additionally reported. TEM and APT contribute significantly to characterize the composition, size and crystallographic structure of individual precipitates. These techniques allow the highest magnification necessary to resolve these phases of interest. However, the analyzed areas and volumes are usually restrained to images around 200 × 200 nm in size and volumes of 200 × 50 × 50 nm, respectively.

Small-angle neutron scattering (SANS) and x-ray absorption spectroscopy (XAS) are advanced characterization techniques which allow studying the nanoparticle dispersion in ODS steels in the macroscopic range. In both SANS and XAS, macroscopic material sections can be analyzed (0.1–1 cm^2), thus providing long-range analysis that offers additional and complementary results to TEM and APT (<100 μm^2). SANS and XAS offer global characterization of the nanoparticle dispersion and secondary phases. SANS is used to measure the size distribution of nano-sized phases in materials, while XAS can chemically characterize them. XAS is subdivided into two main features: X-ray absorption near-edge structure (XANES), which provides information about both

* Corresponding author.
E-mail address: monoro@fis.uc3m.es (M. Oñoro).

https://doi.org/10.1016/j.nme.2024.101671
Received 22 February 2024; Received in revised form 20 April 2024; Accepted 7 May 2024
Available online 9 May 2024

electronic and geometric structure and oxidation states in the analyzed material, and extended x-ray absorption fine-structure (EXAFS), which provides information of the local atomic structure (atomic distances, chemical coordination, etc.) for any atomic elements of interest. This study presents a comprehensive characterization, both morphological and chemical, of nanoprecipitates in the ODS ferritic steel under study, based on a macroscopic analysis domain. TEM and APT or SANS and XAS cannot, on their own, fully elucidate the complex nature of nanoprecipitates and secondary phases in RAF ODS steels. Therefore, this research aims to complement with SANS and XAS techniques the results previously obtained by TEM and APT [5].

Long term operation in fusion nuclear reactors under extreme temperatures may cause the evolution of the already existing phases in the structural material. With this purpose, the thermal stability of the nanoprecipitates and secondary phases is further explored through the application of a thermal aging treatment on the material that simulates the operational temperatures of these facilities. This is essential to attain a full understanding of the scope of application of these structural materials. Several studies have presented the impact of thermal aging treatments on the microstructure and mechanical properties in RAFM (reduced activated ferritic-martensitic) steels (9–12 Cr wt. %) [6–8], but there is still a scarcity of research conducted on Fe-14Cr wt. % (ODS RAF) steels [9–11], as studies taking advantage of techniques as SANS [12,13]. This study aims to provide experimental data on thermal aging experiments to contribute for the validation and development of structural materials as ODS Fe-14Cr (wt%) steels.

2. Experimental

An ODS ferritic alloy was manufactured by mechanical alloying of pre-alloyed atomized Fe–14Cr–2W–0.4Ti (wt. %) powder with $0.3Y_2O_3$ (wt. %) nanosized powder. The milled powder was packed into mild-steel cans and consolidated by hot isostatic pressing (HIP) at 1373 K and 175 MPa for 2 h. The obtained material was subsequently hot cross rolled (HCR) at 1473 K to a thickness reduction of ~ 70 %. Following HCR, the material was annealed at 1273 K for 2 h and air cooled. The material at this step is taken as a reference and denoted as ODS-R. Subsequently, one batch of the alloy was thermally aged at 873 K for 2000 h in an Ar atmosphere and air cooled. This material will be denoted as ODS-A. Additional details about the manufacturing process can be found elsewhere [14,15]. Both ODS-R and ODS-A steels were characterized by SANS and XAS.

A SANS experiment was performed at the ISIS Neutron and Muon Source, in Oxfordshire (UK), using the ZOOM instrument at the Rutherford Appleton Laboratory (experiment RB2310339) [16]. Neutron scattering enables the independent study of the magnetic and nuclear contributions to the scattering intensity. A set of measurements was performed to understand the underlying nanoprecipitate sizes and distribution using SANS. The detector to sample distance was 4 m, the neutron beam size 4 × 4 mm and the beam wavelength varied between 1.75 and 16.5 Å. The Zoom detector is a 1.4 × 1 m rectangle made of 192 tubes 1 m long and 8.1 mm apart, therefore the accessible q-range is not symmetrical in all directions. In addition, the direct beam does not hit the geometrical center of the detector, and the additional shadow is the beamstop arm.

6 × 6 mm squared samples with 1 mm thickness were used for the SANS experiment. The experiment was performed at room temperature (RT), applying a saturating magnetic field of ~ 1.4 T to align the magnetic contributions. This is straightforward in isotropic samples. However, it becomes more difficult to interpret in anisotropic samples as the present material, due to the HCR thermomechanical treatment applied. Thus, pairs of data sets were acquired by varying the sample orientation 90° (perpendicular to the beam axis) for studying anisotropy in the material. These are referred in the text as horizontal and side-on orientation. The scattering intensities were extracted in the directions parallel and perpendicular to the applied magnetic field, averaging over 30° sectors to obtain both the nuclear and the nuclear plus magnetic contributions, respectively. Then, the magnetic scattering can be calculated by subtraction.

The neutron scattering is defined by the scattering momentum transfer wave vector Q, dependent upon the scattering angle θ and neutron wavelength λ:

$$Q = \left|\vec{k}_s - \vec{k}_i\right| = \frac{4\pi}{\lambda}\sin\left(\frac{\theta}{2}\right) \tag{1}$$

where $\vec{k}_i$ and $\vec{k}_s$ are the incident and scattered neutron beam wave vectors, respectively.

SANS measures the scattering from both nuclear and magnetic contributions in the analyzed material. For an isotropic material the nuclear component is radially symmetric. However, the intensity from the magnetic scattering only contributes to the direction perpendicular between the direction of the magnetic moment and the momentum transfer (Q, in equation (1)) as shown in Fig. 1. The magnetization can be aligned along one axis under the presence of an external magnetic field, high enough to saturate the ferromagnetic matrix of the material under study. Thus, the scattering at the perpendicular direction to Q is the sum of the nuclear and magnetic components, while the parallel to Q contains only the nuclear scattering. This allows both contributions to be separated.

In the particle matrix approximation, SANS intensity can be expressed in terms of the macroscopic differential scattering cross section [17]:

$$\frac{d\Sigma}{d\Omega}(Q) \sim f_p\left[\Delta\rho^2_{nucl} + \Delta\rho^2_{mag}\sin^2\alpha\right]F^2(Q,R,h(R))S(Q,R) \tag{2}$$

where f_p is the atomic fraction of precipitates, α indicates the angle between Q and the magnetization of the sample, $F(Q,R)$ its form factor and $h(R)$ its size distribution, $S(Q,R)$ is an interference term (for concentrations below a few percent is equal to one) and $\Delta\rho_{nucl,mag}$ are the nuclear or magnetic contrasts, respectively. The nuclear and magnetic contrasts are given by the expression:

$$\Delta\rho_{nucl,mag} = \frac{b^p_{nucl,mag}}{\nu^p_{at}} - \frac{b^m_{nucl,mag}}{\nu^m_{at}} \tag{3}$$

where $b^{p,m}_{nucl,mag}$ is the nuclear or magnetic mean scattering length, respectively, and $\nu^{p,m}_{at}$ the mean atomic volume regarding the precipitates, p, or the matrix, m.

The nuclear mean scattering length of the precipitates and the matrix is defined by the following expression:

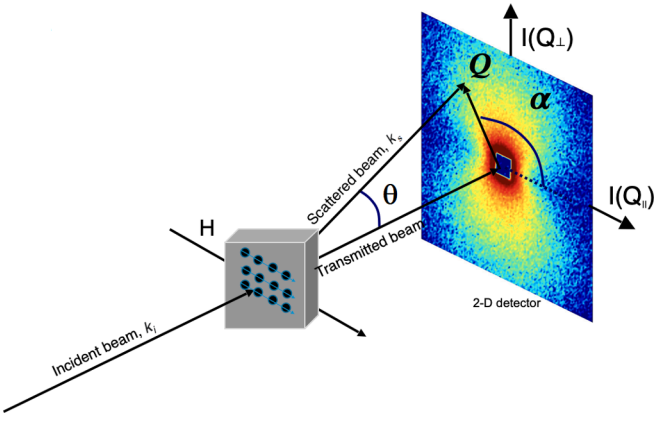

Fig. 1. SANS vectorial representation over a typical scattering pattern. $I(Q_\perp)$ and $I(Q_{||})$ represents the scattering intensities perpendicular and parallel to applied magnetic field, H, respectively.

$$b_{nucl}^{p,m} = \sum_i b_i(C_i) \tag{4}$$

where $b_i(C_i)$ represents the individual nuclear scattering lengths (Table 1) of the main chemical elements weighted over their respective relative concentrations [14].

The magnetic mean scattering length of the matrix is determined by:

$$b_{mag}^{m} = -\gamma \frac{r_0}{2}\mu \tag{5}$$

where $\gamma = -1.913$ is the neutron gyromagnetic factor, $r_0 = 0.2818{\cdot}10^{-12} cm$ is the classical electron radius and μ is the mean magnetic moment of the atoms.

The mean magnetic scattering for the matrix has been calculated considering only the magnetic contributions of iron and chromium. It is assumed that only chromium atoms concentration is relevant [17] (other alloying elements contribute in comparison in a low amount to the total matrix content), consisting of a different magnetic moment than iron atoms. Thus, the mean magnetic moment of the system (μ) is estimated with the relation:

$$\mu = \mu_{Fe} - 2.39 C_{Cr} \tag{6}$$

where $\mu_{Fe} = 2.217$ is the magnetic moment of Fe in Bohr magneton units [20,21]; and C_{Cr} is the chromium atomic concentration. The mean magnetic scattering for the secondary phases under study (oxide nanoparticles) is considered equal to 0, since they are non-magnetic precipitates [22].

Matrix mean atomic volume is obtained from the atomic volumes of the chemical elements of the matrix over the Avogadro number: $\nu_{at}^{m} = 1.179{\cdot}10^{-23} \text{Å}^3$. Precipitates averaged atomic volumes are calculated from CIF files [23,24] and summarized in Table 2.

Under high magnetic field (H) the magnetization of the matrix is saturated, and the magnetic scattering can be experimentally determined from the difference between the scattering intensity contributions for $\alpha = 90^{\circ}$ and $\alpha = 0^{\circ}$ (perpendicular and parallel to H, respectively). The ratio between the magnetic and nuclear sum over the nuclear contribution is defined as the A-ratio (equation (7)). The A-ratio can provide details about chemical composition, magnetization and atomic density for secondary phases with sharp interfaces homogeneously distributed. However, different types of precipitates can present the same result for the A-ratio. In this scenario, additional information, such as TEM or APT, can help to identify the secondary phase type by defining the crystallographic structure and chemical composition, thus highlighting the best candidate for the calculated A-ratio. For a fully saturated material, the A-ratio can be simplified as the second term in equation (7):

$$A = \frac{\left(\frac{d\Sigma}{d\Omega}\right)_{\perp H}}{\left(\frac{d\Sigma}{d\Omega}\right)_{\parallel H}} = 1 + \frac{\Delta\rho_{mag}^2}{\Delta\rho_{nucl}^2} \tag{7}$$

Table 2 presents calculated and bibliographic A-ratios of Y-Ti-O-rich secondary phases, commonly reported in ODS Fe-14Cr (wt. %) steels.

The scattering contrasts and the fitting functions to SANS scattering intensity values offer an estimation of the volume fraction of precipitates and, particularly, of the oxide nanoparticles. Number densities are obtained from volume fractions, considering spherical nanoparticles of radius r, by the relation:

Table 1
Nuclear scattering lengths of the main chemical elements of interest [18,19].

Element	Fe	Cr	W	Ti	Y	O
b (10^{-12} cm)	0.945	0.3635	0.486	−0.337	0.775	0.5803

$$\upsilon = NV = N\frac{4}{3}\pi r^3 \tag{8}$$

where υ is the nanoparticles volume fraction and N the nanoparticles number density.

Fitting functions were made using SasView 5.0.5 [25]. We have described our system as a two-phase model using a power law for representing the scattering stemming from the steel matrix and larger secondary phases, and a Guinier law for the nanoparticles. This first part of the model commonly follows a power law where the scattering function decreases at low momentum transfer (Q). This region includes the contribution of microstructural heterogeneities, around tens of nanometers in size, and grain boundaries. The second contribution of the model for the nanoparticles for higher Q values is based on a Guinier law approximation [26]. Information on the composition, volume fraction and size was obtained. The scale and the radius parameters varied during the fit iterations, and the scattering length density and the scattering length density solvent parameters were constrained. Furthermore, the scattering length density was set based on the nanoparticle chemical composition selected by the study of the experimental A-ratios and the values reported in Table 2.

A XAS experiment was carried out to study the oxidation state and the short-range structure in ODS RAF steels. XAS measurements were performed at ALBA synchrotron light source facility at the BL22-CLAESS beamline, located in Cerdanyola del Vallès (Spain) [28]. Both X-ray Absorption Near-Edge Structure (XANES) and Extended X-ray Absorption Fine Structure (EXAFS) were acquired on the Fe K-edge (7112 eV), the W LIII-edge (10207 eV), and the Y K-edge (17038 eV). Spectra were acquired at RT using a Si(311) double crystal monochromator. The energy resolution attained was 2 eV. XAS spectra for the materials under study were measured in fluorescence mode due to the low concentration of some elements in the samples; additional experimental references were prepared in pellet form and measured in transmission mode: metallic Fe, Y, Y_2O_3 and $Fe_5Y_3O_{12}$. The samples were placed at a 45° tilting angle from the incident beam; the fluorescence signal was collected using a 6 channel SDD detector. To obtain a good signal/noise ratio, 4 scans were collected for each sample. On the other hand, 8 scans were acquired for very low concentration samples to obtain a high-quality k-space data for EXAFS characterization up to 15 Å.

XANES data offers information about the oxidation state of the samples. Reference samples in powder form were used to calibrate the energy values by their correlation with the well-known oxidation states from standards. EXAFS data were fitted in the R-space, from 1.5 to 3.5 Å to scope the signal of two coordination shells. Fitting paths were obtained from CIF files of references [24]. First, the reference samples were fitted to calculate the energy shift (ΔE_0) and the passive electron reduction factor (S_0^2) parameters for each element. ΔE_0 calibrates the energy grid of the experimental spectrum [29] with the theoretical calculated spectrum. S_0^2 is an experimental parameter that evaluates the quantity of electron excitations without contribution to the fine structure [30]. The calculated value of S_0^2 was linked to the effective coordination number of neighbors in the reference samples, as both are fully correlated in the EXAFS equation [31].

ODS-R and ODS-A samples were characterized on the absorption Fe K-edge, Y K-edge and W LIII-edge. The measurements were performed under fluorescence geometry. EXAFS spectra were acquired in Y K-edge and W LIII-edge up to $k = 15.5$ Å^{-1} and $k = 16.4$ Å^{-1} respectively. For Fe K-edge only XANES region was measured up to $k = 7$ Å^{-1}.

XAS data were analyzed using the Demeter package standard procedure [32]. Data reduction, background subtraction and normalization were performed using the Athena software [32]. EXAFS data analysis was carried out using the Artemis software. EXAFS oscillations were extracted using the AUTOBK algorithm, employing a spline in the range from 0 to 15 Å^{-1} k-range having a R_{bkg} of 1.3. Hanning based windows were used to obtain the Fourier transform. The FEFF 6.0 code was used

Table 2
Calculated and bibliographic A-ratios for Y-Ti-O-rich secondary phases in a Fe-14Cr (wt. %) matrix.

Secondary Phase	Structure	V_{at} (cm^3)	$\Delta\rho^2_{nucl}$(cm^{-4})	$\Delta\rho^2_{mag}$(cm^{-4})	A-ratio
$(Y+Ti)_2O_3$	[17]	$1.49{\cdot}10^{-23}$	$2.23{\cdot}10^{21}$	$1.85{\cdot}10^{21}$	1.95
YTiO	[17]	$1.17{\cdot}10^{-23}$	$1.87{\cdot}10^{21}$	$1.85{\cdot}10^{21}$	1.99
$Y_2Ti_2O_7$	Monoclinic P121	$1.32{\cdot}10^{-23}$	$1.46{\cdot}10^{21}$	$1.85{\cdot}10^{21}$	2.27
$Y_2Ti_2O_7$	Cubic Fd $\bar{3}$ m2	$1.22{\cdot}10^{-23}$	$1.25{\cdot}10^{21}$	$1.85{\cdot}10^{21}$	2.48
$Y_2Ti_2O_7$	Monoclinic C12/m1	$1.17{\cdot}10^{-23}$	$1.15{\cdot}10^{21}$	$1.85{\cdot}10^{21}$	2.60
Y_2TiO_5	Orthorhombic $Pn2_1a$	$1.35{\cdot}10^{-23}$	$1.16{\cdot}10^{21}$	$1.85{\cdot}10^{21}$	2.59
$YTiO_{2.085}$	Cubic Fd $\bar{3}$ m2	$1.61{\cdot}10^{-23}$	$2.24{\cdot}10^{21}$	$1.85{\cdot}10^{21}$	1.83
YTi_3O_6	Triclinic P $\bar{1}$	$1.31{\cdot}10^{-23}$	$2.26{\cdot}10^{21}$	$1.85{\cdot}10^{21}$	1.82
YTi_2O_4	Tetragonal $I4_1/a$	$1.21{\cdot}10^{-23}$	$1.91{\cdot}10^{21}$	$1.85{\cdot}10^{21}$	1.97
YTi_2O_4	Orthorhombic Pnma	$1.26{\cdot}10^{-23}$	$2.01{\cdot}10^{21}$	$1.85{\cdot}10^{21}$	1.92
YTi_2O_4	Cubic Fd $\bar{3}$ m1	$1.27{\cdot}10^{-23}$	$2.03{\cdot}10^{21}$	$1.85{\cdot}10^{21}$	1.91
YTi_2O_4	Orthorhombic Pnma	$1.23{\cdot}10^{-23}$	$1.94{\cdot}10^{21}$	$1.85{\cdot}10^{21}$	1.95
$YTiO_3$	Orthorhombic −P 2ac 2n	$1.15{\cdot}10^{-23}$	$1.19{\cdot}10^{21}$	$1.85{\cdot}10^{21}$	2.55
$YTiO_3$	Orthorhombic −P 2ac 2n	$1.16{\cdot}10^{-23}$	$1.20{\cdot}10^{21}$	$1.85{\cdot}10^{21}$	2.54
$YTiO_3$	Orthorhombic −P 2ac 2n	$1.15{\cdot}10^{-23}$	$1.18{\cdot}10^{21}$	$1.85{\cdot}10^{21}$	2.57
$YTiO_3$	Hexagonal $P6_3cm$	$1.29{\cdot}10^{-23}$	$1.48{\cdot}10^{21}$	$1.85{\cdot}10^{21}$	2.25
$YTiO_3$	Cubic Pm $\bar{3}$ m1	$1.18{\cdot}10^{-23}$	$1.25{\cdot}10^{21}$	$1.85{\cdot}10^{21}$	2.48
$YTiO_3$	Hexagonal $P6_3/mmc$	$1.30{\cdot}10^{-23}$	$1.51{\cdot}10^{21}$	$1.85{\cdot}10^{21}$	2.23
$Y_2Ti_3O_9$	Orthorhombic Pnma	$1.20{\cdot}10^{-23}$	$1.45{\cdot}10^{21}$	$1.85{\cdot}10^{21}$	2.27
$Y_{16}Ti_{16}O_{35}$	Triclinic P1	$1.31{\cdot}10^{-23}$	$1.70{\cdot}10^{21}$	$1.85{\cdot}10^{21}$	2.09
O-vac-Y-Ti [27]	bcc Fe, O at octahedral sites, Y:Ti ratio 0.2–0.4	–		–	1.41–1.71
CrO [27]	NaCl a = 0.465 nm	–	–	–	2.5
Cr_2O_3 [27]	Hexagonal a = 0.4959 nm, c = 1.359 nm 6 formula units per unit cell	–	–	–	4.9
$Fe_{3.4}Cr_{1.1}Y_{6.9}Ti_{43.9}O_{44.7}$, 10 %vac [27]	NaCl	–	–	–	1.672
0.1 < Y:Ti < 0.6 [27]	–	–	–	–	1.6 – 2–2
$Cr_{4.6}Y_{14.6}Ti_{37.9}O_{42.8}$ [27]	NaCl	–	–	–	2.03
Porosity / nanovoids [27]	–	–	$5.20{\cdot}10^{21}$	$1.78{\cdot}10^{21}$	1.34

for path generation [33,34]. Theoretical paths were fit using a global S_0^2 value and ΔE_0. Single and multiple scattering paths were fit in terms of Δr and σ^2, which represent the deviation from the expected interatomic distances and the structural disorder, respectively. Multi k-weighting (1,2,3) was used to fit EXAFS spectra. To assess the quality of the fits both the R_{factor} and χ^2 were minimized, ensuring that the data were not over-fit.

FEFF 9.6.4 software [35] was used to simulate XANES spectra of Y-based compounds. FEFF is an automated software for ab initio multiple scattering based on a real space Green's function approach for calculation of EXAFS and XANES regions. EXCHANGE card with Hedin-Lundqvist model was employed for the energy dependent exchange correlation potential. SCF card was used with a radius of 5 Å and COREHOLE card with Final State Rule was also selected.

3. Results and discussion

3.1. Small angle neutron scattering

Scattering intensities associated to the nuclear component for both ODS-R and ODS-A steels on the side-on and horizontal orientations are shown in Fig. 2 and Fig. 3, respectively. The nuclear component was extracted in the direction parallel to the applied magnetic field and offers information on the structural characterization of secondary phases being scattering centers. Y-rich nanoparticles present in both ODS-R and ODS-A steels [5] are non-magnetic precipitates, whose contribution is thus linked with the nuclear scattering curves. Fits to scattering curves obtained using SasView software follow a two-phase model (solid lines in Fig. 2), which is the sum of a power law and a Guinier approximation. The dotted lines represent the power law fits linked to bigger precipitates, and the dashed lines the fits based on a Guinier-Law approximation to the oxide nanoparticles (fitting functions and the two-phase model are displayed only in Fig. 2 for an easier visualization of other figures).

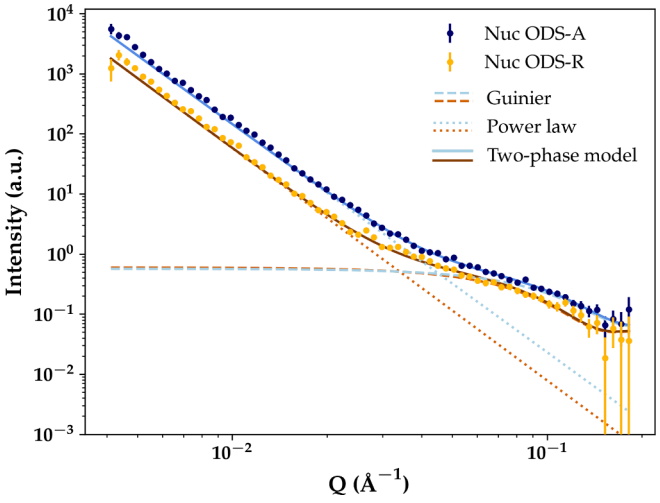

Fig. 2. Nuclear scattered intensity measured on ODS-R and ODS-A and fitting functions on the side-on sample orientation. The two-phase model (solid line) represents the sum of the power law fit (dotted line) and the Guinier approximation (dashed line).

The thermal aging treatment applied to ODS-A had no discernible impact on the scattering signal related to the oxide nanodispersion (Guinier approximation). This is evidenced in the scattering curves (and fitting functions), which show only minor deviations in the side-on orientation (Fig. 2) and overlap on the horizontal configuration (Fig. 3). This highlights the stability of these precipitates under the aging

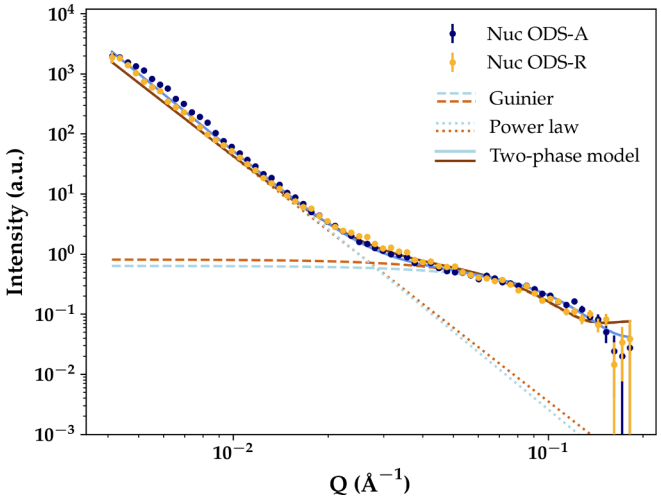

Fig. 3. Nuclear scattered intensity measured on ODS-R and ODS-A and fitting functions on the horizontal sample orientation. The two-phase model (solid line) represents the sum of the power law fit (dotted line) and the Guinier approximation (dashed line).

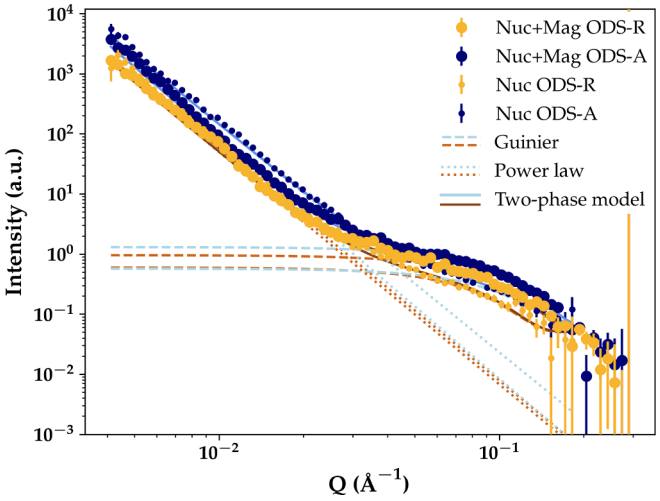

Fig. 5. Scattered intensity measured on ODS-R and ODS-A and fitting functions on the side-on sample orientation. The two-phase model (solid line) represents the sum of the power law fit (dotted line) and the Guinier approximation (dashed line).

treatment applied, as previously reported [5]. Following thermal aging, the power law region indicates higher nuclear scattering intensities on the side-on orientation for ODS-A (Fig. 2), while remaining very similar on the horizontal configuration (Fig. 3). The deviation between ODS-R and ODS-A in the power law region at the side-on orientation is explored through the study of the magnetic scattering influence.

A 2D SANS scattering pattern for the ODS-A steel sample is depicted in Fig. 4(a). The study of the magnetic scattering offers additional information on scattering centers with magnetic properties. ODS-R and ODS-A showed no magnetic contribution on the side-on orientation (Fig. 5), although they do show magnetic scattering on the horizontal configuration (Fig. 6). This behavior could be related to the microstructure anisotropy induced by the HCR treatment [14,36,37]. In Fig. 6, both steel samples manifest similar magnetic scattering at the Guinier region and the intensity in ODS-A is higher than in ODS-R at the power law approximation. This increase in the scattering for ODS-A might come from the presence of magnetic secondary phases not present in ODS-R. Based on the study reported in [5], large magnetic secondary phases are associated to the growth of the magnetic Laves phase following the direction of the HCR along grain boundaries after thermal aging in ODS-A.

On the side-on configuration (Fig. 5), the external magnetic field is applied perpendicularly to the rolling direction, which means perpendicular to the elongated grains, grain boundaries and Laves phase. The saturation of these magnetic scattering centers is more difficult to attain at this geometry because of their morphological anisotropy. The steel matrix in both ODS-R and ODS-A is saturated, but the applied magnetic field of 1.4 T may not be enough to attain the complete saturation of the Laves phase in ODS-A. Thus, the magnetic contribution to the scattering intensity in the direction parallel to the applied magnetic field might not be zero and the nuclear scattering intensity would be biased. This might be the reason for the nuclear component of ODS-A in Fig. 5 being slightly higher than the sum of the nuclear and the magnetic signals. This behavior is restrained to the power law region, which may support that it is associated to the Laves phase. Then, the higher intensity observed in ODS-A respect to ODS-R in Fig. 2 is also linked to this behavior rather than being associated to the formation of new scattering centers.

These nuclear and magnetic components (Fig. 5 and Fig. 6) are used to calculate the A-ratios following equation (7). The A-ratios for ODS-R and ODS-A on the side-on and horizonal configurations are presented in Fig. 7 and Fig. 8, respectively. They show A-ratios for all the Q range. However, the A-ratios for the oxide nanoparticles were obtained from

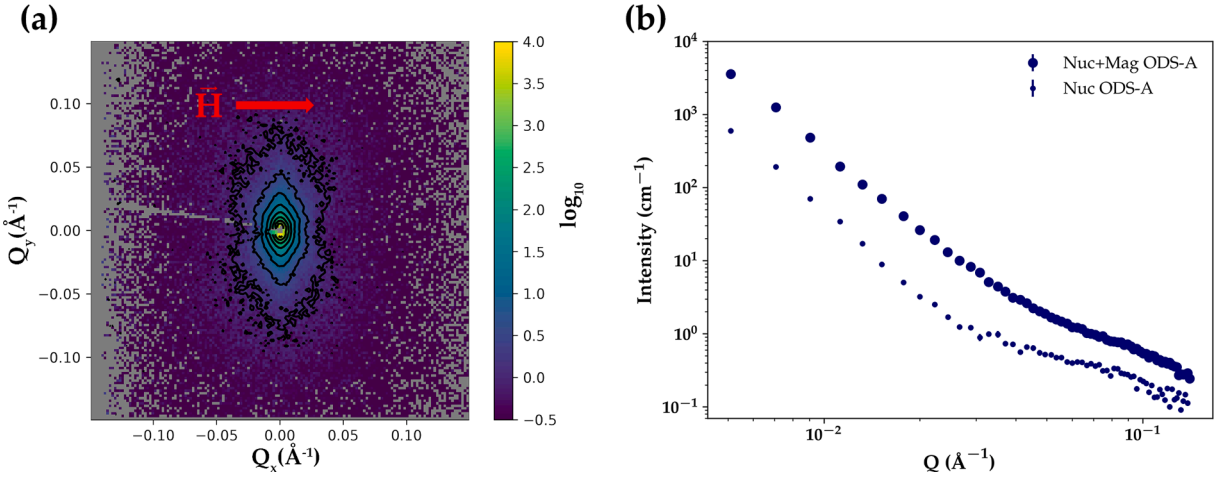

Fig. 4. (a) A 2D SANS scattering pattern contour plot with the magnetic field perpendicular to the incident beam on ODS-A. (b) Nuclear plus magnetic and nuclear components for ODS-A obtained from (a).

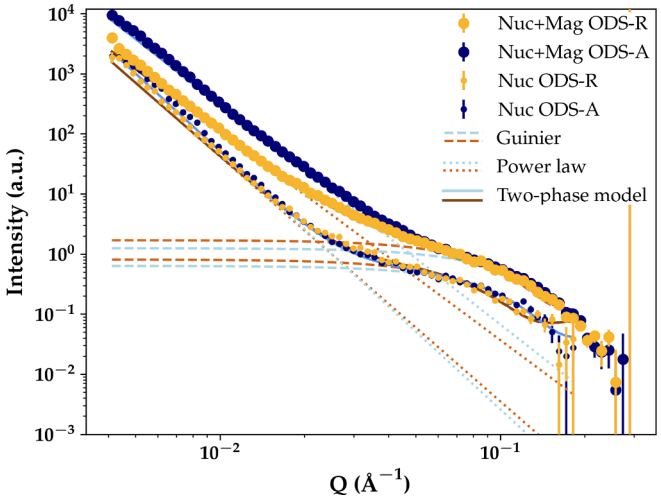

Fig. 6. Scattered intensity measured on ODS-R and ODS-A and fitting functions on the horizontal sample orientation. The two-phase model (solid line) represents the sum of the power law fit (dotted line) and the Guinier approximation (dashed line).

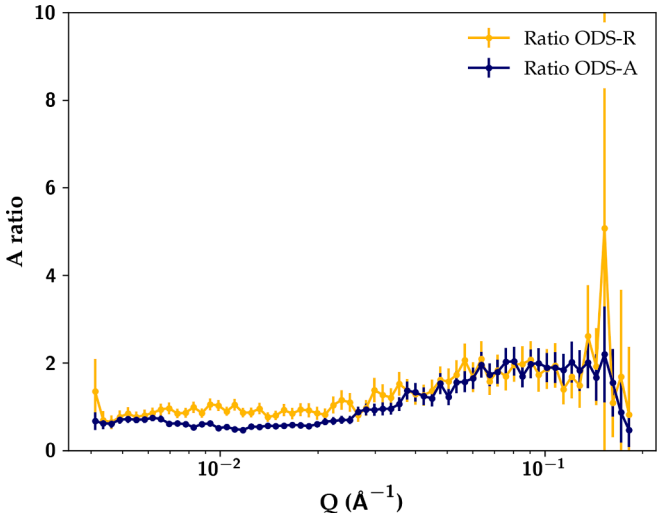

Fig. 7. A-ratio for ODS-R and ODS-A on the side-on sample orientation.

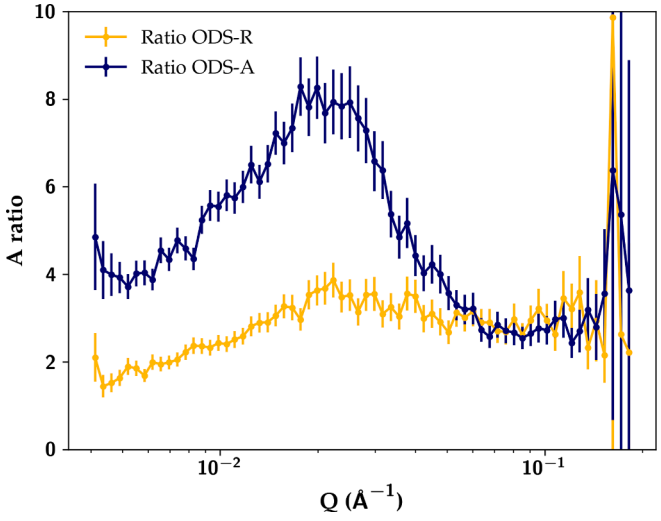

Fig. 8. A-ratio for ODS-R and ODS-A on the horizontal sample orientation.

Table 3
SANS results obtained on ODS-R and ODS-A for the horizontal configuration for the nanoparticle dispersion. A-ratio, mean radius, R_m, volume fraction, V_f, and number density, N.

Sample	A-ratio	R_m (nm)	V_f (%)	N (m^{-3})
ODS-R	2.9 ± 0.2	2.45 ± 0.04	0.96 ± 0.03	(1.56 ± 0.05)·10^{23}
ODS-A	2.7 ± 0.3	2.19 ± 0.04	1.19 ± 0.03	(2.70 ± 0.07)·10^{23}

the Guinier-Law approximation fitting functions of the two-phase model (Table 3), where A-ratios remain constant (Fig. 7 and Fig. 8). The biased results regarding the nuclear component in ODS-A on the side-on orientation restrict the A-ratio analysis to the horizontal configuration in both steels.

The A-ratio on the horizontal orientation was 2.9 ± 0.2 for ODS-R and 2.7 ± 0.3 for ODS-A. In Table 2, the calculated A-ratio for $Y_2Ti_2O_7$ was 2.60 and for Y_2TiO_5 was 2.59. Thus, the experimental A-ratios for both ODS-R and ODS-A show close agreement with both $Y_2Ti_2O_7$ and Y_2TiO_5 phases. Previous TEM studies identified some nanoparticles in ODS-R or ODS-A as Y_2TiO_5 [5].

Volume fraction and mean radii were obtained from Guinier fitting functions using SasView software. The scattering length density was set to zero and the scattering length density solvent parameters to 3.4·10^{-6} Å^{-2} based on the results summarized in Table 2 for the $Y_2Ti_2O_7$ and Y_2TiO_5 phases. Volume fraction of nanoparticles resulted as 0.96 ± 0.03 % for ODS-R and 1.19 ± 0.04 % for ODS-A, and a mean radius that lowered after thermal aging for ODS-A to 2.19 ± 0.04 nm, respect to 2.45 ± 0.04 nm for ODS-R. Then, based on the assumption of spherical nanoparticles, their number densities were calculated, showing an increase up to (2.70 ± 0.07)·10^{23} m^{-3} for ODS-A, from (1.56 ± 0.05)·10^{23} m^{-3} for ODS-R.

The A-ratios at the power law approximation region for the side-on orientation (Fig. 7) display values below one as the nuclear intensity was higher than the sum of the nuclear and magnetic scattering as previously discussed and reported in Fig. 5. However, the results obtained on the horizontal configuration (Fig. 8) differ drastically. The substantial increase observed for the A-ratio in ODS-A might be associated again to the precipitation of the magnetic Laves phase after thermal aging anisotropically distributed in the steel matrix, as also observed in Fig. 6. Further research and new experiments are necessary to elucidate and confirm the mechanisms associated to this particular outcome.

To further explore microstructural anisotropies in ODS-A and ODS-R samples, additional measurements are represented in Fig. 9. The nuclear scattering obtained for ODS-R does not present any sign of anisotropy as a function of the sample orientation (Fig. 9(a)). The hot rolling treatment (HCR) applied on these materials induced an anisotropic distribution of the ferritic grains in the steel matrix [14] and, consequently, an anisotropic configuration of grain boundaries. However, the grain boundary anisotropy produced by the HCR treatment was not visible in Fig. 9(a).The sum of the nuclear and the magnetic scatterings for ODS-R is higher at the horizontal than at the side-on sample orientation (Fig. 9 (b)). This difference in the intensity was identified as a magnetic contribution due to the microstructure induced anisotropy in the material.

Comparing both orientations in ODS-A, the regions of higher Q values present isotropic distribution of nanoparticles, for both nuclear and the sum of the nuclear and the magnetic scattering (Fig. 9(c) and (d), respectively). Additionally, it is worth noting the substantial differences in the scattering intensities at lower Q values. First, the nuclear anisotropy was attributed to a bias contribution of magnetic scattering from the Laves phase not being fully saturated on the side-on orientation. Second, the sum of the nuclear and magnetic scatterings also presents anisotropic behavior in the same region of Q values (Fig. 9(d)). This is associated to a drastic increase of the magnetic contribution due to the presence of the occurring Laves phase with a preferential orientation after thermal aging.

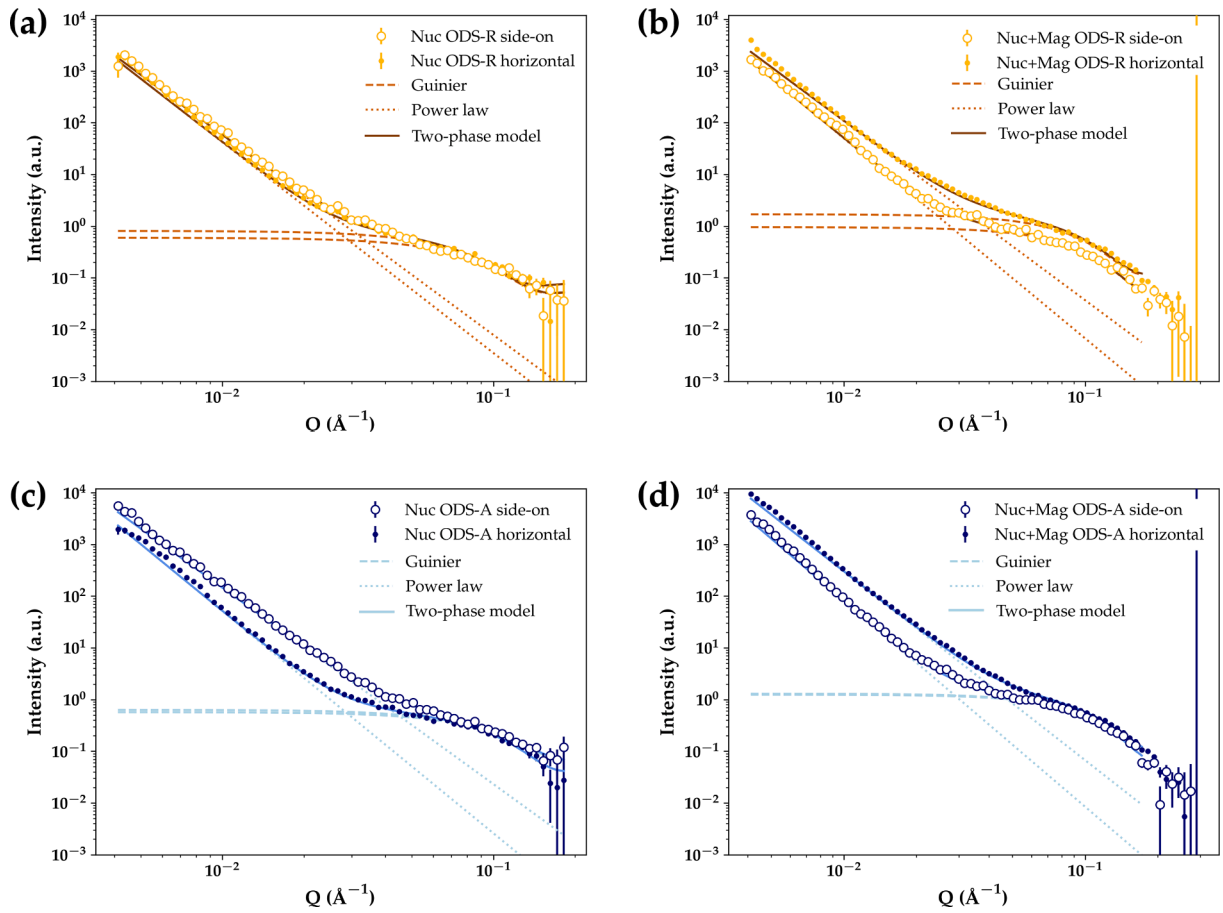

Fig. 9. Nuclear and nuclear plus magnetic SANS scattered intensities and fitting functions at two different sample orientations (a) and (b) ODS-R and (c) and (d) ODS-A. The two-phase model (solid line) represents the sum of the power law fit (dotted line) and the Guinier approximation (dashed line).

3.2. X-ray absorption spectroscopy

3.2.1. X-ray absorption near-edge structure – XANES

An iron metallic sample was measured as reference in transmission mode; the calculated energy absorption on the Fe K-edge for both ODS-R and ODS-A corresponds to the expected 7112 eV for metallic iron. Iron atoms in both ODS-R and ODS-A mainly form metallic bonds, highlighting the metallic character of both steels (Fig. 10).

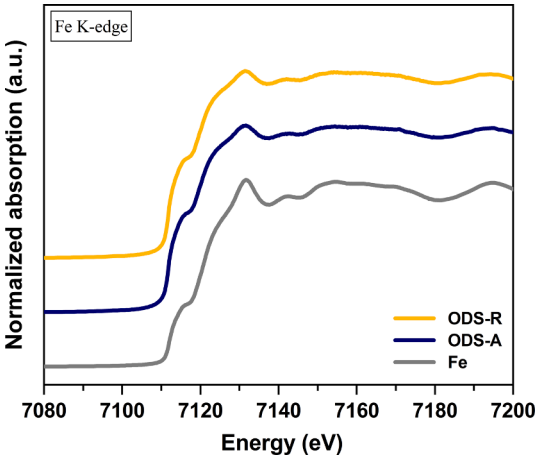

Fig. 10. Normalized XANES spectra on the Fe K-edge for ODS-R and ODS-A samples and Fe experimental reference.

The experimental results on the Y K-edge for ODS-R and ODS-A are depicted in Fig. 11 and Fig. 12. In Fig. 11 three additional experimental spectra of metallic Y, Y_2O_3 and $Fe_5Y_3O_{12}$ references are included. These phases are used to illustrate three different references as a metallic phase, an oxide and an additional oxide with a more complex structure like in the Y-rich nanoprecipitates. The energy at the absorption edge for metallic yttrium is 17038.0 eV, for Y_2O_3 (Y^{3+}) is 17043.5 eV and for $Fe_5Y_3O_{12}$ (Y^{3+}) is 17043.0 eV. An absorption energy of 17043.3 eV was obtained for ODS-R, and a value of 17042.5 eV for ODS-A. These results offer mean oxidation states of 2.8+ and 2.6+ for ODS-R and ODS-A,

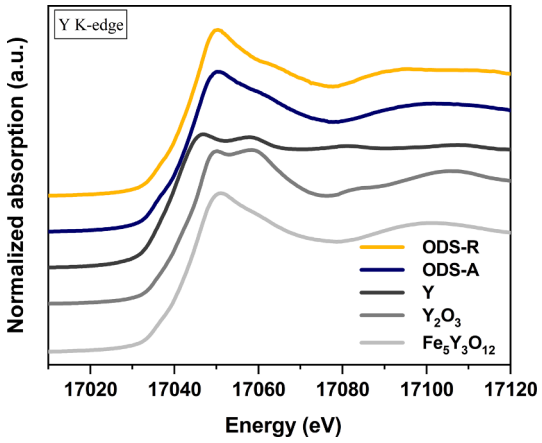

Fig. 11. Normalized XANES spectra on the Y K-edge of ODS-R and ODS-A together with the metallic Y, Y_2O_3 and $Fe_5Y_3O_{12}$ experimental references.

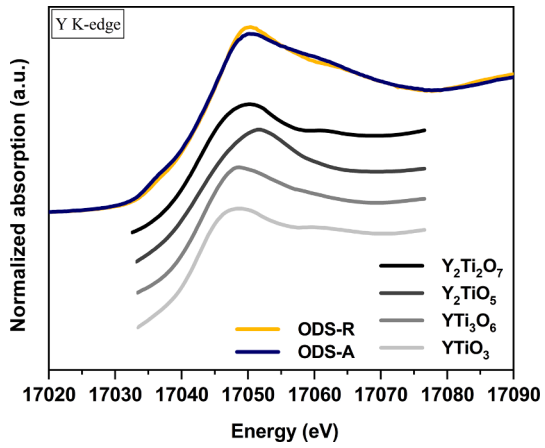

Fig. 12. Normalized XANES on the Y K-edge of ODS-R and ODS-A together with the simulated spectra for $Y_2Ti_2O_7$, Y_2TiO_5, YTi_3O_6 and $YTiO_3$.

respectively. It was previously reported by TEM and APT analysis ([5,37]) that yttrium mainly forms Y-rich nanoprecipitates as Y_2TiO_5 (Y^{3+}) or non-stoichiometric phases. The observed oxidation states, below the expected 3+ value in a perfect structure, may indicate that there is a small proportion of metallic yttrium in the materials or, at the same time, the presence of non-stoichiometric Y-rich phases (as the nanoprecipitates) where the electronic levels are not fully occupied. Metallic yttrium was not reported in ODS- R nor in ODS-A; therefore, these results might relate to the non-stoichiometry of the Y-rich nanoparticles.

Fig. 12 includes the simulated XANES obtained with the FEFF software using CIF files [24] for $Y_2Ti_2O_7$ (M.P.: 5373), Y_2TiO_5 (M.P.: 17559), YTi_3O_6 (M.P.: 1045032) and $YTiO_3$ (M.P.: 4355). $Y_2Ti_2O_7$ and Y_2TiO_5 are the most common crystallographic structures reported in the literature [38,39] for Y-rich nanoparticles in ODS steels. In [5], Y_2TiO_5 was reported for nanoparticles over 5 nm in size, while smaller nanoparticles were non-stoichiometric, as confirmed by APT studies in this same material [5]; $Y_2Ti_2O_7$ was not reported neither in ODS-R or ODS-A (although it is considered for comparison purposes [40]). TEM image analysis showed 96 % of nanoparticles being < 5 nm in size in ODS-R and 95 % in ODS-A; APT showed 100 % of the nanoparticles as < 5 nm in ODS-R and 95 % in ODS-A. Thus, the interpretation of the Y K-edge signals is based on the contribution study of Y_2TiO_5 and $Y_2Ti_2O_7$ [41]; the contribution of non-stoichiometric nanoparticles of varying sizes is difficult to infer but may play a major role [42].

ODS-R spectrum is similar to the simulated Y_2TiO_5; ODS-A, presenting a second substructure, resembles the simulated $Y_2Ti_2O_7$ or $YTiO_3$, which also presents a second substructure centered at 17063 eV and 17061 eV, respectively. This could be interpreted as the effect of thermal aging decreasing the contribution of the Y_2TiO_5 signal at macroscopic scale, maybe favoring $Y_2Ti_2O_7$, $YTiO_3$ or other different crystal structures similar to these ones that could not be identified in this research. APT analysis presented in [5] showed a mean Y/Ti ratio for nanoprecipitates of 1.6 ± 1.1 for ODS-R and a lower value of 1.2 ± 0.7 for ODS-A. This analysis of the XANES results shows a similar trend, since the expected predominant phase in ODS-R, Y_2TiO_5, has a Y/Ti ratio of 2, in agreement with the APT result, while in ODS-A, the expected $Y_2Ti_2O_7$ and $YTiO_3$ phases have a Y/Ti ratio of 1, close to the 1.2 value from APT in this same steel. Considering the previously mentioned restrictions, the XANES results on the Y K-edge signal on ODS-R and ODS-A point out to Y-rich compounds that are consistent with the APT analysis previously reported.

Overlapping both normalized XANES spectra of ODS-R and ODS-A, some small differences could be appreciated between them in Fig. 12. On the absorption edge, there is a small change in the tendency of the slope on the onset of the curve between 17030 and 17040 eV. Over the absorption edge, the maximum absorption peak at 17050 eV is slightly higher for the ODS-R due to small differences in the electronic structure between ODS-R and ODS-A.

ODS-R and ODS-A were characterized on the absorption W LIII-edge (Fig. 13). Metallic tungsten was additionally measured and used as reference. WO_3 and WO_2 spectra were obtained in a different experiment and illustrate two compounds with different oxidation states. Metallic tungsten had an absorption edge energy of 10207 eV, WO_2 (W^{4+}) 10207.7 eV and WO_3 (W^{6+}) 10209.2 eV. The absorption edge energies for ODS-R and ODS-A were 10207 and 10207.1 eV, respectively. This suggests a high metallic state of tungsten atoms for both ODS-R and ODS-A.

The presence of W-Cr-rich secondary phases was reported in both ODS-R and ODS-A and they were identified as $M_{23}C_6$ carbides. The presence of Laves phases (WFe_2) was identified by a multi-technique characterization in ODS-A ([5]). FEFF software was used to simulate the XANES spectra of these two phases of interest based on their respective CIF files. Particularly, the $M_{23}C_6$ CIF file was modified to obtain a chemical composition proportion matching the ThermoCalc® simulations reported for these precipitates [5]. The modified stoichiometry from ThermoCalc® simulations was $Cr_{17}W_3Fe_3C_6$. Fig. 13 summarizes the experimental and simulated results. ODS-R XANES is comparable to the simulated $Cr_{17}W_3Fe_3C_6$ (they exhibit a similar trend between 10215–10230 eV), while ODS-A resembles a combination of both $Cr_{17}W_3Fe_3C_6$ and WFe_2 (with a higher slope between 10215–10230 eV in these cases), where the Laves phase WFe_2 could represent a minor but noticeable contribution.

3.2.2. *Extended x-ray absorption fine-structure – EXAFS*

The module of the Fourier transforms for ODS-R and ODS-A, representing the EXAFS oscillations on the Y K-edge as a function of the distance, are depicted in Fig. 14. Fitting functions obtained with the Artemis software are also represented. The $Fe_5Y_3O_{12}$ reference was used to adjust the experimental values for ODS-R and ODS-A. The amplitudes, $S_0^2 = 0.805$, and the energies, $\Delta E_0 = -7.06$ eV, were also obtained by this method. Experimental data were fitted in the R range between 1.6 to 3.9 Å. The fitting functions assume a first shell configured by two different O neighbors signals, and a second shell with a single contribution of Fe atoms. In the first shell, the first O signal with $N = 4$ is centered on 2.382 Å and the second with $N = 4$ on 2.469 Å; in the second shell, the combination of Fe + Y signals is centered on 3.459 Å for fitting purposes. Table 4 summarizes the results describing number of neighbors, atomic species and atomic distances for ODS-R and ODS-A as well as theoretical values computed for reference oxides.

The number of first O neighbors was 6.0 ± 0.8 for ODS-R and 6.5 ± 0.3 for ODS-A; mean distance values stay stable with minor differences.

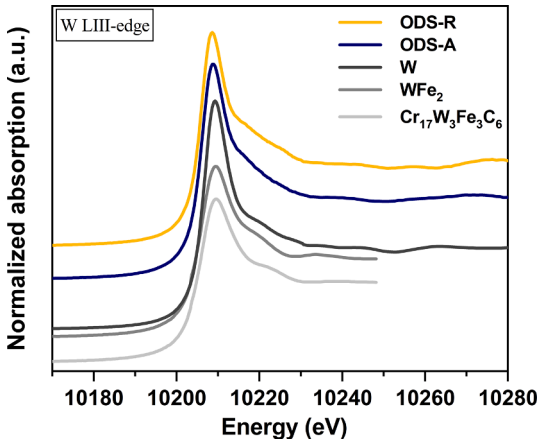

Fig. 13. Normalized XANES spectra on the W LIII-edge of ODS-R and ODS-A together with the metallic W, and the simulated WFe_2 and $Cr_{17}W_3Fe_3C_6$.

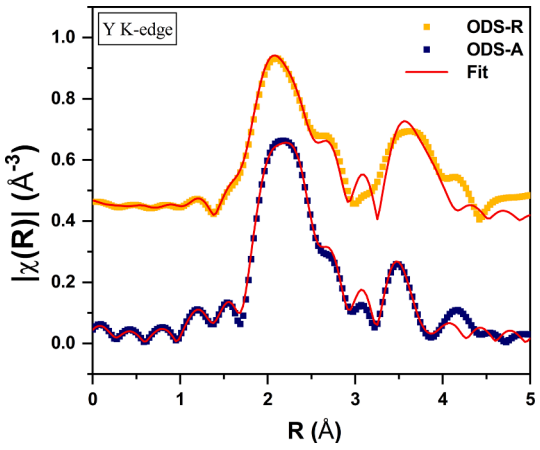

Fig. 14. Fourier transform magnitude of k^2-weighted EXAFS oscillations on the Y K-edge for ODS-R, ODS-A and their respective fits. First Y-O scattering path from Y_2O_3 has been used for phase correction. Experimental data were fitted in the R range between 1.6 and 3.9 Å.

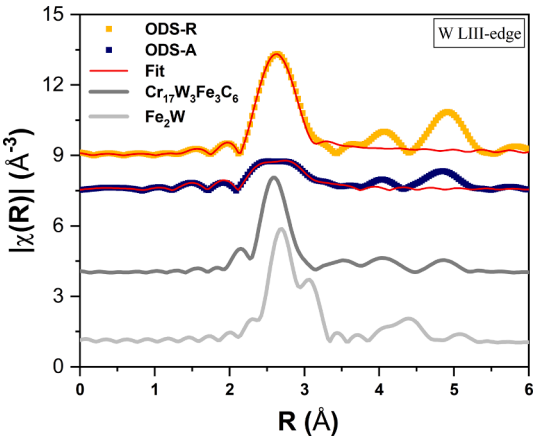

Fig. 15. Fourier transform magnitude of k^2-weighted EXAFS oscillations on the W LIII-edge for ODS-R, ODS-A, their respective fits, and the simulated WFe_2 and $Cr_{17}W_3Fe_3C_6$. First W-Fe scattering path from Fe_2W has been used for phase correction. Experimental data were fitted in the R range between 2.1 and 3.4 Å.

For both ODS-R and ODS-A, the number of O first neighbors is lower than the two references used in this study, Y_2TiO_5 and $Y_2Ti_2O_7$; this, again, might show the big influence of both nanometric sizes and non-stoichiometry regarding the oxide precipitates. Nanometric and non-stoichiometric precipitates might be favored to have a higher number of vacancies and, thus, empty neighbors that would reduce the O signal from first O neighbors.

After thermal aging, the number of first O neighbors increases from 6.0 ± 0.8 to 6.5 ± 0.3. This could be associated with an increase of the contribution of $Y_2Ti_2O_7$ (or a similar compatible phase as $YTiO_3$), which has a higher number of oxygen atoms as first neighbors, eight (also eight for $YTiO_3$), compared to Y_2TiO_5 (seven). This behavior follows the same trend presented with XANES where Y_2TiO_5 was more predominant than $Y_2Ti_2O_7$ in ODS-R, and the opposite for ODS-A. At the same time, this trend could also be associated to a decrease in the signal from non-stoichiometric nanoparticles in favor of well-defined Y_2TiO_5 (or partially $Y_2Ti_2O_7$, or even both structures at the same time) that approaches the number of O neighbors to the expected value of 7 for Y_2TiO_5 without overtaking it. Both TEM and APT analysis in [5] pointed out to the dissolution of small nanoparticles after aging. Thus, the contribution of the biggest nanoparticles reported as Y_2TiO_5 on TEM diffraction analysis may gain importance, in agreement with the increment of O first neighbors shown by EXAFS.

The ratio of first O neighbors between the first and second shells in ODS-R follows a similar relation to the expected Y_2TiO_5. ODS-A follows the same trend linked to the presence of Y_2TiO_5, which is the opposite tendency of $Y_2Ti_2O_7$, where the second shell is the most occupied. On the other hand, mean distances in both ODS-R and ODS-A differ between their respective first and second shells, when the first and second shells in Y_2TiO_5 are very similar and they are not in $Y_2Ti_2O_7$. Non-stoichiometric phases could have a considerable number of atoms slightly shifted from their equilibrium positions that could increase their interatomic distances, as it has been observed.

The EXAFS oscillations obtained through the Fourier transform on the W LIII-edge for simulated samples, ODS-R and ODS-A, with their respective fitting functions, are depicted in Fig. 15. The model used assumes a first shell that includes three signals of first neighbors: C atoms with N = 2 centered at 2.122 Å, Fe and/or W atoms with N = 11 between 2.364 and 2.876 Å and W atoms with N = 1 centered at 2.526 Å. The metallic W reference measured was used to calibrate the experimental results for ODS-R and ODS-A. $S_0^2 = 0.921$ and $\Delta E_0 = 6.75$ eV were additionally obtained by this method. Experimental data were fitted in the R range between 2.1 and 3.4 Å. The fitting functions for the first cells in both ODS-R and ODS-A steels exhibit a high degree of agreement with the experimental data (Fig. 15).

The presence of the $M_{23}C_6$ phase as Cr-W-rich precipitates was reported in [5] in both ODS-R and ODS-A steels, while Laves phase

Table 4
Experimental and theoretical EXAFS results and values on the Y K-edge.

Sample	Element	N	R_{eff} (Å)	σ^2 (Å^2)	R-factor
ODS-R	**O1**	3.5(3)	2.24(1)	0.004(1)	0.0556
experimental	**O2**	2.5(5)	2.42(2)	0.004(2)	
	Total O	6.0(8)	2.31(2)		
	Y + Ti	9.3(4.2)	3.61(1)	0.001(3)	
ODS-A	**O1**	4.4(1)	2.23(1)	0.004(1)	0.0099
experimental	**O2**	2.1(2)	2.40(1)	0.002(1)	
	Total O	6.5(3)	2.28(1)		
	Y + Ti	9.5(3.7)	3.57(1)	0.006(3)	
Y_2TiO_5	**O1**	4	2.357		
theoretical (M.P.: 17559)	**O2**	3	2.371		
	Total O	7	2.363		
	Y + Ti	10	3.635		
$Y_2Ti_2O_7$	**O1**	2	2.206		
theoretical (M.P.: 5373)	**O2**	6	2.502		
	Total O	8	2.428		
	Y + Ti	12	3.602		
Y_2O_3	**O**	6	2.304		
theoretical (M.P.: 2652)	**Y**	6	3.557		

Table 5
Experimental and theoretical EXAFS results and values on the W LIII-edge.

Sample	Element	N	R_{eff} (Å)	σ^2 (Å^2)	R-factor
ODS-R	**C**	1.8(2.2)	2.03(1)	0.003(3)	0.0176
experimental	**Cr + Fe**	15.8(1.3)	2.56(1)	0.003(1)	
	W	1.6(1.2)	2.78(1)	0.004(5)	
ODS-A	**C**	1.5(6)	2.74(1)	0.002(3)	0.0097
experimental	**Cr + Fe**	6.3(3)	2.60(1)	0.0017(2)	
	W	0.6(4)	2.47(1)	0.002(2)	
	Fe	4.0(2)	2.78(1)	0.0018(4)	
	W	1.8(6)	2.78(1)	0.002(1)	
$Cr_{17}W_3Fe_3C_6$	**C**	2	2.112		
theoretical	**Cr + Fe**	11	2.599		
(modified M.P.: 723)	**W**	1	2.526		
WFe_2	**Fe**	12	2.766		
theoretical	**W**	4	2.890		
(M.P.: 20868)					

occurred during the aging treatment and its presence was only reported on the ODS-A sample. Therefore, the EXAFS oscillations obtained from the ODS-R sample were exclusively modeled with the signal of the $Cr_{17}W_3Fe_3C_6$ phase (described in the previous section); and the model for the ODS-A material included a second additional contribution of the WFe_2 phase. The CIF file used for the study of the WFe_2 phase has the first neighbor contributions of Fe atoms with N = 12 and an average distance of 2.766 Å and W atoms with N = 4 at 2.890 Å.

Table 5 summarizes and compares these results. The $Cr_{17}W_3Fe_3C_6$ phase, based on a $M_{23}C_6$ CIF file (M.P.: 723), perfectly fits the experimental results obtained for the ODS-R sample. The number of first metallic neighbors (Cr + Fe) for the ODS-R steel is higher than the expected by the carbide phase. This might be an indication of the presence of other Fe/Cr/W-rich metallic phases with different stoichiometries in the steel matrix of ODS-R. After thermal aging, the EXAFS oscillations of W-rich phases in ODS-A appears as the sum of two different contributions. Thus, the linear combination fitting function for ODS-A of the $Cr_{17}W_3Fe_3C_6$ and WFe_2 (M.P.: 20868) structures shows the same contribution around 50 % for each phase. These results further confirmed the formation of the Laves phase during thermal aging as reported by XRD, EBSD and TEM [5] and by SANS in section 3.1.

The number of first metallic neighbors (Cr + Fe) in ODS-A related to the $Cr_{17}W_3Fe_3C_6$ phase is lower than ODS-R and even lower than the $Cr_{17}W_3Fe_3C_6$ reference itself. First C atoms remain similar as the ODS-R steel and the $Cr_{17}W_3Fe_3C_6$ reference. Regarding the Laves phase formation in ODS-A, the number of first W atoms is slightly lower than expected compared to the WFe_2 reference, and the number of first Fe atoms is clearly lower than the anticipated.

4. Conclusions

SANS and XAS experiments have been performed to characterize the thermal stability of the oxide nanoparticle dispersion in the ODS steels under study and to obtain further information regarding formation of secondary phases after long-term aging. SANS and XAS show the highest potential for the comprehensive characterization of nanoparticles and secondary phases in ODS steels, allowing for the characterization of macroscopic volumes, which provide a global characterization of the materials. The final conclusions can be summarized as follows:

- The dispersion of oxide nanoparticles is isotropic in both ODS-R and ODS-A, and stable after thermal aging.
- The oxide nanoparticles composition showed close agreement with both Y_2TiO_5 and $Y_2Ti_2O_7$ phases by the results on the experimental and calculated A-ratios in both ODS-R and ODS-A. The mean radius for the nanoparticles slightly lowered after thermal aging, while the number density increased, but showing an overall stability.
- ODS-A showed strong magnetic anisotropies, not observed in ODS-R. This was associated to Laves phase precipitation, with a preferential orientation along grain boundaries in ODS-A after thermal aging.
- Yttrium atoms show mean oxidation states of 2.8+ and 2.6+ for ODS-R and ODS-A, respectively. This may point out the presence of non-stoichiometric Y-rich nanoprecipitates, whose electronic levels are not fully occupied respect to the expected oxidation state of 3+ as in $Y_2Ti_2O_7$, Y_2TiO_5 or $YTiO_3$. EXAFS analysis shows a reduced number of O neighbors, related to nanometric and non-stoichiometric precipitates.
- The EXAFS oscillations on the W LIII-edge for ODS-R highly resemble the modified $Cr_{17}W_3Fe_3C_6$ phase. After thermal aging, the good agreement between the experimental results and the fitting function shows that ODS-A may be the result of two different contributions: the $Cr_{17}W_3Fe_3C_6$ carbide and the WFe_2 Laves phase.

CRediT authorship contribution statement

M. Oñoro: Writing – review & editing, Writing – original draft, Visualization, Investigation, Formal analysis, Data curation, Conceptualization. **S.R. Parnell:** Writing – review & editing, Visualization, Supervision, Methodology, Investigation, Formal analysis, Data curation, Conceptualization. **E. Salas-Colera:** Writing – review & editing, Writing – original draft, Visualization, Supervision, Methodology, Investigation, Formal analysis, Data curation, Conceptualization. **D. Alba Venero:** Writing – review & editing, Visualization, Investigation, Formal analysis. **V. Martin-Diaconesu:** Writing – review & editing, Visualization, Investigation, Formal analysis. **T. Leguey:** Writing – review & editing, Investigation, Funding acquisition, Formal analysis, Conceptualization. **V. de Castro:** Writing – review & editing, Investigation, Funding acquisition, Formal analysis, Conceptualization. **M.A. Auger:** Writing – review & editing, Visualization, Validation, Supervision, Methodology, Investigation, Funding acquisition, Formal analysis, Conceptualization.

Declaration of competing interest

The authors declare that they have no known competing financial interests or personal relationships that could have appeared to influence the work reported in this paper.

Data availability

Data will be made available on request.

Acknowledgements

Funding from AEI (Agencia Estatal de Investigación) with reference AEI/10.13039/501100011033 (project PID2019-105325RB-C33); Comunidad de Madrid (Spain) through the programs Talento-CAM

(2017-T1/IND-5439 and 2021-5A/IND-20954), Technofusion (III) CM (S2018/EMT-4437) and multiannual agreements with UC3M ("Excelencia para el Profesorado Universitario"-EPUC3M14 and "Fostering Young Doctors Research" NANOSOLREC programs); and the V PRICIT (Research and Technological Innovation Regional Program) is gratefully acknowledged. Funding for APC was granted by Universidad Carlos III de Madrid (Agreement CRUE-Madroño 2024). Prof. Dr. Ir. J. Sietsma is acknowledged for providing constructive comments to this work. This work benefited from the use of the SasView application, originally developed under NSF award DMR-0520547. SasView also contains code developed with funding from the European Union's Horizon 2020 research and innovation programme under the SINE2020 project, grant agreement No 654000. Authors thank ALBA-CLAESS staff for providing support during experiment ID: 2021095333.

References

[1] S.J. Zinkle, J.P. Blanchard, R.W. Callis, C.E. Kessel, R.J. Kurtz, P.J. Lee, K. A. McCarthy, N.B. Morley, F. Najmabadi, R.E. Nygren, G.R. Tynan, D.G. Whyte, R. S. Willms, B.D. Wirth, Fusion materials science and technology research opportunities now and during the ITER era, Fusion Eng. Des. 89 (2014) 1579–1585, https://doi.org/10.1016/j.fusengdes.2014.02.048.

[2] N. Baluc, D.S. Gelles, S. Jitsukawa, A. Kimura, R.L. Klueh, G.R. Odette, B. van der Schaaf, J. Yu, Status of reduced activation ferritic/martensitic steel development, J. Nucl. Mater. 367–370 (Part A) (2007) 33–41, https://doi.org/10.1016/J.JNUCMAT.2007.03.036.

[3] M.J. Alinger, G.R. Odette, D.T. Hoelzer, On the role of alloy composition and processing parameters in nanocluster formation and dispersion strengthening in nanostuctured ferritic alloys, Acta Mater. 57 (2009) 392–406, https://doi.org/10.1016/J.ACTAMAT.2008.09.025.

[4] N. Baluc, J.L. Boutard, S.L. Dudarev, M. Rieth, J.B. Correia, B. Fournier, J. Henry, F. Legendre, T. Leguey, M. Lewandowska, R. Lindau, E. Marquis, A. Muñoz, B. Radiguet, Z. Oksiuta, Review on the EFDA work programme on nano-structured ODS RAF steels, J. Nucl. Mater. 417 (2011) 149–153, https://doi.org/10.1016/j.jnucmat.2010.12.065.

[5] M. Oñoro, V. de Castro, T. Leguey, J. Pöpperlová, R.M. Huizenga, M.A. Auger, Microstructural stability of secondary phases in an ODS ferritic steel after thermal aging at 873 K, Mater Charact 207 (2024), https://doi.org/10.1016/J.MATCHAR.2023.113517.

[6] B.R. Sun, A.D. Zhou, Y.L. Li, Z.L. Zhang, C.C. Du, S.X.Y. Gu, Z. Chen, X.C. Cai, S. W. Xin, T.D. Shen, Ultrafine-grained oxide-dispersion-strengthened 9Cr steel with exceptional strength and thermal stability, Nucl. Mater. Energy 30 (2022), https://doi.org/10.1016/J.NME.2021.101112.

[7] P. Zheng, Y. Li, J. Zhang, J. Shen, T. Nagasaka, T. Muroga, H. Abe, On the thermal stability of a 9Cr-ODS steel aged at 700 °C up to 10000 h - Mechanical properties and microstructure, Mater. Sci. Eng. A 783 (2020), https://doi.org/10.1016/J.MSEA.2020.139292.

[8] Q. Min, Q. Guo-xing, C. Ming-chong, D. Qing, C. Lei, W. Hong-yan, Microstructure stability and mechanical properties of reduced activated ferritic martensitic steel during thermal aging at 550 °C for 5000 h, J. Mater. Eng. Perform. 32 (2023) 5410–5420, https://doi.org/10.1007/S11665-022-07498-6.

[9] Y. Wen, Y. Liu, D. Liu, B. Tang, Preparation and thermal stability of a mechanically alloyed oxide dispersion strengthened ferritic steels, Mater. Sci. Forum 715–716 (2012) 605–610, https://doi.org/10.4028/WWW.SCIENTIFIC.NET/MSF.715-716.605.

[10] S.F. Li, Z.J. Zhou, P.H. Wang, H.Y. Sun, M. Wang, G.M. Zhang, Long-term thermal-aging stability of a 16Cr-oxide dispersion strengthened ferritic steel at 973 K, Mater Des 90 (2016) 318–329, https://doi.org/10.1016/J.MATDES.2015.10.138.

[11] J.S. Lee, C.H. Jang, I.S. Kim, A. Kimura, Embrittlement and hardening during thermal aging of high Cr oxide dispersion strengthened alloys, J. Nucl. Mater. 367–370 (2007) 229–233, https://doi.org/10.1016/J.JNUCMAT.2007.03.007.

[12] P.-L. Gao, J. Gong, Q. Tian, G.-A. Sun, H.-Y. Yan, L. Chen, L.-F. Bai, Z.-M. Guo, X. Ju, Small-angle neutron scattering study on the stability of oxide nanoparticles in long-term thermally aged 9Cr-oxide dispersion strengthened steel, Chin. Phys. 31 (2022), https://doi.org/10.1088/1674-1056/AC43AA.

[13] S.Y. Zhong, J. Ribis, V. Klosek, Y. De Carlan, N. Lochet, V. Ji, M.H. Mathon, Study of the thermal stability of nanoparticle distributions in an oxide dispersion strengthened (ODS) ferritic alloys, J. Nucl. Mater. 428 (2012) 154–159, https://doi.org/10.1016/J.JNUCMAT.2011.12.028.

[14] M. Oñoro, J. Macías-Delgado, M.A. Auger, V. de Castro, T. Leguey, Mechanical properties and stability of precipitates of an ODS steel after thermal cycling and aging, Nucl. Mater. Energy 24 (2020), https://doi.org/10.1016/j.nme.2020.100758.

[15] J. Macías-Delgado, Microestructura y propiedades mecánicas de aceros de activación reducida endurecidos mediante dispersión de óxidos, Tesis Doctoral (2019). http://hdl.handle.net/10016/29747.

[16] Dr Diego Alba Venero, Mr Moises Oñoro, Dr Steven Parnell, SANS study of the nanosized features in oxide dispersion strengthened alloys, ISIS Neutron and Muon Source Data Journal (n.d.). https://doi.org//10.5286/ISIS.E.RB2310339-1.

[17] M.H. Mathon, M. Perrut, S.Y. Zhong, Y. De Carlan, Small angle neutron scattering study of martensitic/ferritic ODS alloys, J. Nucl. Mater. 428 (2012) 147–153, https://doi.org/10.1016/J.JNUCMAT.2011.12.010.

[18] H. Börner, J. Brown, C.J. Carlile, R. Cubitt, R. Currat, A.J. Dianoux, B. Farago, A. Hewat, J. Kulda, E. Lelièvre-Berna, G. McIntyre, S.A. Mason, R.P. May, A. Oed, J.R. Stewart, F. Tasset, J. Tribolet, R.S. Eccleston, M. Johnson, C.C. Wilson -ISIS, G. Lander, H. Rauch, W. Waschkowski, A. Mader, Neutron Data Booklet, (2003). https://www.ill.eu/fileadmin/user_upload/ILL/1_About_ILL/Documentation/NeutronDataBooklet.pdf.

[19] V.F. Sears, Neutron scattering lengths and cross sections, Neutron News 3 (1992) 26–37, https://doi.org/10.1080/10448639208218770.

[20] A.T. Aldred, Ferromagnetism in iron-chromium alloys. I. Bulk magnetization measurements, Phys. Rev. B 14 (1976) 219, https://doi.org/10.1103/PhysRevB.14.219.

[21] A.T. Aldred, B.D. Rainford, J.S. Kouvcl, T.J. Hicks, Ferromagnetism in iron-chromium alloys. II. Neutron scattering studies*, accessed April 20, 2024, Phys. Rev. B 14 (1976), https://journals.aps.org/prb/pdf/10.1103/PhysRevB.14.228.

[22] J.M.D. Coey, D.H. Ryan, Current trends in amorphous magnetism, IEEE Trans. Magn. 20 (1984) 1278–1283, https://doi.org/10.1109/TMAG.1984.1063532.

[23] A. Merkys, A. Vaitkus, A. Grybauskas, A. Konovalovas, M. Quirós, S. Gražulis, Graph isomorphism-based algorithm for cross-checking chemical and crystallographic descriptions, J. Cheminformat. 15 (2023) 1–13, https://doi.org/10.1186/S13321-023-00692-1.

[24] A. Jain, P. Shyue, G. Ong, W.C. Hautier, D. William, S. Richards, S. Dacek, D. Cholia, D. Gunter, G. Skinner, K.A. Ceder, S.P. Persson, W.D.R. Ong, The materials project: a materials genome approach to accelerating materials innovation, APL Mater. 17 (2023), https://doi.org/10.1063/1.4812323.

[25] SasView for Small Angle Scattering Analysis, (n.d.). https://www.sasview.org/help/.

[26] A. Guinier, C.B. Walker, N. York, J. Wiley, Small-angle scattering of X-rays, Wiley (1955), https://doi.org/10.1126/science.123.3197.591.c.

[27] I. Hilger, F. Bergner, A. Ulbricht, A. Wagner, T. Weißgärber, B. Kieback, C. Heintze, C.D. Dewhurst, Investigation of spark plasma sintered oxide-dispersion strengthened steels by means of small-angle neutron scattering, J. Alloy. Compd. 685 (2016) 927–935, https://doi.org/10.1016/J.JALLCOM.2016.06.238.

[28] L. Simonelli, C. Marini, W. Olszewski, M. Ávila Pérez, N. Ramanan, G. Guilera, V. Cuartero, K. Klementiev, CLÆSS: The hard X-ray absorption beamline of the ALBA CELLS synchrotron, Cogent Phys. 3 (2016), https://doi.org/10.1080/23311940.2016.1231987.

[29] S.D. Kelly, B. Ravel, EXAFS Energy shift and structural parameters, AIP Conf. Proc. 882 (2007) 132–134, https://doi.org/10.1063/1.2644451.

[30] J.J. Rehr, E.A. Stern, R.L. Martin, E.R. Davidson, Extended x-ray-absorption fine-structure amplitudes—Wave-function relaxation and chemical effects, Phys. Rev. B 17 (1978) 560, https://doi.org/10.1103/PhysRevB.17.560.

[31] D.C. Koningsberger, Roelof. Prins, X-ray absorption : principles, applications, techniques of EXAFS, SEXAFS, and XANES, Wiley, 1988. https://www.wiley.com/en-gb/X+Ray+Absorption%3A+Principles%2C+Applications%2C+Techniques+of+EXAFS%2C+SEXAFS+and+XANES+-p-9780471875475.

[32] B. Ravel, M. Newville, ATHENA, ARTEMIS, HEPHAESTUS: data analysis for X-ray absorption spectroscopy using IFEFFIT, J. Synchrotron Radiat. 12 (Pt 4) (2005) 537–541, https://doi.org/10.1107/S0909049505012719.

[33] J.J. Rehr, R.C. Albers, Theoretical approaches to x-ray absorption fine structure, Rev. Mod. Phys. 72 (2000) 621, https://doi.org/10.1103/RevModPhys.72.621.

[34] M. Newville, EXAFS analysis using FEFF and FEFFIT, J. Synchrotron Radiat. 8 (2001) 96–100, https://doi.org/10.1107/S0909049500016290.

[35] J.J. Rehr, J.J. Kas, F.D. Vila, M.P. Prange, K. Jorissen, Parameter-free calculations of X-ray spectra with FEFF9, PCCP 12 (2010) 5503–5513, https://doi.org/10.1039/B926434E.

[36] M. Oñoro, T. Leguey, V. de Castro, M.A. Auger, Effects of thermal aging at 873 K on the impact properties of an ODS ferritic steel, Nucl. Mater. Energy 36 (2023), https://doi.org/10.1016/J.NME.2023.101455.

[37] M. Oñoro, J. Macías-Delgado, M.A. Auger, J. Hoffmann, V. de Castro, T. Leguey, Powder particle size effects on microstructure and mechanical properties of mechanically alloyed ODS ferritic steels, Metals 12 (2021) 69, https://doi.org/10.3390/MET12010069.

[38] G. Robert Odette, N.J. Cunningham, T. Stan, M. Ershadul Alam, Y. De Carlan, Nano-Oxide Dispersion-Strengthened Steels, in: Structural Alloys for Nuclear Energy Applications, Elsevier, 2019: pp. 529–583. Doi: 10.1016/B978-0-12-397046-6.00012-5.

[39] D.T. Hoelzer, J. Bentley, M.A. Sokolov, M.K. Miller, G.R. Odette, M.J. Alinger, Influence of particle dispersions on the high-temperature strength of ferritic alloys, J. Nucl. Mater. 367–370 (Part A) (2007) 166–172, https://doi.org/10.1016/j.jnucmat.2007.03.151.

[40] S. Liu, C.U. Segre, G.R. Odette, Characterization of oxide dispersion-strengthened steels by x-ray absorption spectroscopy, in: Transaction of the American Nuclear Society, 2008: p. 1067. https://www.researchgate.net/publication/224975629.

[41] S. Liu, G.R. Odette, C.U. Segre, Evidence for core–shell nanoclusters in oxygen dispersion strengthened steels measured using X-ray absorption spectroscopy, J. Nucl. Mater. 445 (2014) 50–56, https://doi.org/10.1016/J.JNUCMAT.2013.10.042.

[42] A. Hirata, T. Fujita, Y.R. Wen, J.H. Schneibel, C.T. Liu, M.W. Chen, Atomic structure of nanoclusters in oxide-dispersion-strengthened steels, Nat. Mater. 10 (2011) 922–926, https://doi.org/10.1038/nmat3150.